RSC Advances

PAPER

View Article Online
View Journal | View Issue

Cite this: *RSC Adv.*, 2021, **11**, 29287

Dehydrogenation of methylcyclohexane over Pt-based catalysts supported on functional granular activated carbon†

Hong-Li Ye,[ab] Shuang-Xi Liu,[bc] Cui Zhang,*[bc] You-Qiong Cai[a] and Yong-Fu Shi*[a]

Herein, we developed the dehydrogenation of methylcyclohexane over Pt-based catalysts supported on functional granular activated carbon. Sulphuric acid, hydrogen peroxide, nitric acid and aminopropyl triethoxy silane were adopted to modify the granular activated carbon. The structural characterizations suggested that the carbon materials had a large surface area, abundant pore structure, and a high number of oxygen-containing functional groups, which influenced the Pt-based catalysts on the particle size, dispersion and dehydrogenation activity. The hydrogen temperature-programmed reduction technique was utilized to investigate the interaction between the active component Pt and the various functionalized granular activated carbon materials. The CO pulse technique revealed the particle sizes and dispersion of the as-prepared Pt-based catalysts. Finally, the Pt-based catalysts were successfully applied to study their catalytic activity in the dehydrogenation reaction of methylcyclohexane. The results showed that the Pt-based catalyst over granular activated carbon functionalized with sulphuric acid groups had a higher conversion of methylcyclohexane (63%) and a larger hydrogen evolution rate (741.1 mmol g_{Pt}^{-1} min^{-1}) than the other resulting Pt-based catalysts at 300 °C.

Received 17th July 2021
Accepted 20th August 2021

DOI: 10.1039/d1ra05480e

rsc.li/rsc-advances

Introduction

Owing to the cleanliness, rich reserves, environment friendly and high combustion calorific value, hydrogen energy has attracted extensive attention as an alternative energy.[1–5] The global demand for H_2 has increased continuously by 3–4% annually.[6] The flammability of hydrogen results in potential hazards during its storage and transportation. Hence, it is significant to develop a relatively mild and safe storage approach. Liquid organic hydrides have emerged as one of these promising hydrogen carriers owing to their advantages, such as their reversible hydrogenation–dehydrogenation cycles, easy storage and the release of hydrogen on demand *via* the catalytic process, high hydrogen storage capacity, high energy density, convenient transportation in the safe conditions, *etc.*[7–10]

A series of liquid organic hydrides have been developed by cyclohexane, methylcyclohexane (MCH), 1,4-dimethylcyclohexane, and decalin for their high hydrogen storage capacity (6–8%) and high boiling points (80–200 °C) to ensure they are in liquid state during transportation. Among them, MCH is a potential and satisfactory candidate due to its high reversibility and the low toxicity of the dehydrogenation products.[11,12] The dehydrogenation reaction of MCH will be accelerated the reaction process and reduced the activation energy in the presence of catalysts. The active components of the dehydrogenation catalysts are Pt, Pd, Re, Ni, Cu, Co, La, especially the precious metals Pt and Pd. Shukla *et al.*[13] reported that Pt-based catalysts showed a higher activity than the Pd-based catalysts for the dehydrogenation of MCH. Moreover, Pt-based catalysts can selectively activate the C–H bond without cleavage of the C–C bond and dramatically decrease the activation energy.[14,15] What's more, the rate of H spillover on Pt is more rapid than that on Pd, which effectively inhibits the background reaction.[16] The catalyst supports play a significant role in the activity and stability of the Pt-based catalysts. Many efforts have been made on the supports for Pt-based catalysts,[17–20] especially Al_2O_3,[21,22] and activated carbon materials (ACM),[23–26] including activated carbons (AC), activated carbon filters (ACF), activated carbon nanotubes (ACN) and so on. Compared with Al_2O_3, ACM always possesses a high specific surface area, large pore volume and controllable surface, which are beneficial to the dispersion of catalysts.[27] Wang *et al.*[28] showed that the catalytic activity of

[a]*Laboratory of Aquatic Product Quality, Safety and Processing, East China Sea Fisheries Research Institute, Chinese Academy of Fishery Sciences, Shanghai, 200090, China. E-mail: shiyf@ecsf.ac.cn*

[b]*Institute of New Catalytic Materials Science, MOE Key Laboratory of Advanced Energy Materials Chemistry, School of Materials Science and Engineering, National Institute of Advanced Materials, Nankai University, Tianjin 300350, China. E-mail: zhangcui@nankai.edu.cn*

[c]*Collaborative Innovation Center of Chemical Science and Engineering, Tianjin 300072, China*

† Electronic supplementary information (ESI) available. See DOI: 10.1039/d1ra05480e

0.25% Pt/ACN was equal to that of 1% Pt/Al_2O_3. Furthermore, ACM can be modified by HNO_3 and O_3 to increase the number of surface functional groups, which is another factor affecting the dispersion and activity of the catalysts. Viscardi *et al.*[29] reported an MCM-41 sulfonated catalyst with great thermal stability, high surface area, abundant acid loading and the maximum methanol conversion. Hosseini *et al.*[30] adopted sulfonic acid groups to modify the surface of reduced graphene oxide, which formed efficient solid acids with excellent catalytic efficiencies in acetalization and esterification reactions.

Herein, we investigated the dehydrogenation of MCH over Pt-based catalysts supported on functional granular activated carbon (GAC). Sulphuric acid, hydrogen peroxide, nitric acid and aminopropyl triethoxy silane were used to modify the GAC to yield GAC-S, GAC-HO, GAC-N and GAC-NH, respectively. The structural characterization results, including analysis performed using scanning electron microscopy (SEM), Fourier transform infrared spectroscopy (FTIR), N_2-adsorption, X-ray photoelectron spectroscopy (XPS) and thermogravimetric analysis (TGA), suggested that the carbon supports had large surface area, abundant pore structure, and a significant number of oxygen-containing functional groups, which influenced the particle size, dispersion and dehydrogenation activity of the Pt-based catalysts. The hydrogen temperature-programmed reduction (H_2-TPR) technique was utilized to investigate the interaction between the active component Pt and the distinct functionalized granular activated carbon. The CO pulse technique revealed the particle sizes and the dispersion of the as-prepared Pt-based catalysts. Finally, the catalytic activities of the Pt-based catalysts for the dehydrogenation reaction of MCH were studied. The results showed that the Pt/GAC-S catalyst demonstrated a higher conversion of MCH (63%) and a larger hydrogen evolution rate (741.1 mmol g_{Pt}^{-1} min^{-1}) than the other resulting Pt-based catalysts at 300 °C.

Experimental section

Materials

Chloroplatinic acid solution ($H_2PtCl_6 \cdot 6H_2O$) and ethylene glycol solution were purchased from Tianjin Jinhai Type Science and Technology Development Co. Ltd and Tianjin Jiangtian Chemical Technology Co. Ltd, respectively. GAC was provided by Fujian Xin Charcoal Industry Co., Ltd. MCH, toluene (TOL), aminopropyl triethoxy silane, nitric acid, sulphuric acid, and hydrogen peroxide were purchased from Tianjin Concord Technology Co., Ltd. Milli-Q water (18.2 MΩ cm) was utilized throughout the experiments.

Instrumentations

The SEM images were captured by a JEOL JSM-7500F (JEOL, Japan). The Brunauer–Emmett–Teller (BET) specific surface area and the pore structure of the materials were obtained using a microspores instrument ASAP 2020 (American). FTIR spectra were recorded adopting a Vector 22 FTIR spectrophotometer (Bruker, Germany). XPS data were measured utilizing a Kratos Axis Ultra DLD multi-technique with Mg-Kα radiation. All of the measurements were performed at room temperature. X-ray diffraction (XRD) patterns were measured on a Bruker D8 FOCUS diffractometer in the 2θ range of 10–80° (scanning rate of 6° min^{-1} in steps of 0.02°) with Cu K_α (λ = 0.15406 nm) radiation operating at 40 kV and 40 mA. TGA and differential thermogravimetry (DTG) were implemented with a Rigaku thermogravimetry-differential thermal analyzer in nitrogen with a heating rate of 10 °C min^{-1}. The load capacity of Pt was determined using inductively coupled plasma-atomic emission spectrometry (ICP-AES, ICP-9000(N+M)).

Preparation of the functional GAC supports

10 g of GAC was modified by dilute sulfuric acid, aminopropyl triethoxy silane, nitric acid, and hydrogen peroxide with a concentration of 2 mol L^{-1} for 8 h at 65 °C, then washed with deionized water, and dried at 110 °C for 12 h, and marked as GAC-S, GAC-NH, GAC-N, and GAC-HO, respectively.

Preparation of the Pt-based catalysts

Pt-based catalysts were prepared using a previously reported method.[31] Briefly, 2.0 g GAC and 20 mL deionized water were dispersed into a 100 mL three-well flask. After stirring evenly, a certain amount of chloroplatinic acid was dropped into the suspension. Being stirred for 30 min later, 20 mL of ethylene glycol solution was added. The precursor was heated and refluxed for 4 h, then filtered and washed with deionized water. The as-prepared solid was finally dried in a vacuum oven for 12 h at 55 °C to yield Pt/GAC. The loaded amount of Pt in the catalysts was about 0.2% (measured by ICP-AES). The catalysts of Pt/GAC-S, Pt/GAC-HO, Pt/GAC-N and Pt/GAC-NH were synthesized using the same operation. Before the dehydrogenation reaction of MCH was performed, the Pt-based catalysts were reduced using H_2 at 400 °C for 2 h.

He-temperature-programmed decomposition (He-TPD) characterization

He-TPD tests were carried out on a Micromeritics Chemsorb 2750 in a helium gas atmosphere. About 0.20 g of the sample was placed in a U-shaped quartz tube and pretreated in He gas for 1 h at 150 °C before the test, then cooled to 100 °C. Desorption of the sample was performed in the temperature range of 100–1000 °C with a heating rate of 10 °C min^{-1}, and the spectra were recorded.

H_2-TPR characterization

The H_2-TPR technique was also carried out on the Micromeritics Chemsorb 2750 equipped with a thermal conductivity detector. About 0.10 g of the sample was placed into a quartz U-shaped tube and purged for 0.5 h with 10% H_2 in Ar, then heated to 900 °C with a heating rate of 10 °C min^{-1} and the spectra were recorded on a computer.

CO pulse characterization

The CO pulse technique was conducted on a Micromeritics Chemsorb 2750 equipped with a thermal conductivity detector. About 0.10 g of the sample was acquired and reduced by H_2 at 400 °C for 40 min, then cooled to 25 °C under helium protection. The adsorption of CO was begun when the temperature stabilized at 25 °C.

Catalytic reaction

Dehydrogenation of MCH to yield hydrogen and toluene was carried out under atmospheric pressure in a fixed-bed flow reactor (10 mm inner diameter (ID) × 250 mm) with 0.30 g of the Pt-based catalysts. The MCH was injected into the reactor with a pump under a nitrogen stream with a flow rate of 0.03 mL min^{-1}. The conversion of MCH was determined using a Rock GC 7800 gas chromatograph equipped with a flame ionization detector and an SE-30 column.

Recycling studies

Recycling assays were carried out to investigate the heterogeneity and stability of the catalysts. After the first catalytic reaction had finished, the Pt/GAC-S catalyst was recovered by filtration, washed with distilled water, dried at 55 °C for 12 h in a vacuum and reused for the second catalytic reaction. The same operations were implemented in another three runs. At the same time, after the first run, the amount of Pt in the recovered Pt/GAC-S and in the filtrate was detected by ICP-AES.

Results and discussion

Structural characterization of the supports

SEM images displayed the morphology of GAC, as shown in Fig. 1A. GAC appeared as a large number of amorphous spherical particles with a uniform size. The XRD pattern (Fig. 1B) revealed the crystal structure of GAC. The diffraction peaks at 24° and 44° were stemmed from the (002) crystal plane and the (100) crystal plane of graphite microcrystalline (PDF# 041-1487), respectively. The Raman spectrum further evidenced the degree of crystallization of GAC. As revealed in Fig. 1C, the peak at 1334 cm^{-1} for the D band and the 1590 cm^{-1} peak representing the G band were observed in the Raman spectrum of GAC, which were attributed to the disordered carbon and the E_g vibration of the sp^2 bonded carbon double bonds, respectively.[32] Meanwhile, the ratio of I_D/I_G was employed to evaluate the disorder of the material structure.[33] The ratio value of I_D *versus* I_G was calculated to be 1.05, which indicated that the amorphous carbon was a little higher than the crystal carbon in GAC. In addition, 2679 cm^{-1} peak of 2D (an overtone of the D bond) was determined in the Raman spectrum of GAC, which was in agreement with the reported literature.[34] The FTIR spectrum (Fig. 1D) confirmed the abundant oxygen-containing functional groups on the surface of GAC. The peak at 620 cm^{-1} was assigned to the bending vibration of C–H. The absorption peak at 1630 cm^{-1} was assigned to the C=O stretching vibration.[35] 1274 cm^{-1} and 1098 cm^{-1} were attributed to the stretching vibration of C–O–C and the asymmetric stretching vibration of C–OH, respectively.[36,37] The 3130–3740 cm^{-1} region was resulted from the O–H stretching vibration.[38]

The XPS spectra further evidenced the surface structure of GAC. As observed in Fig. 2A, the surface of GAC was composed of a great number of C and O elements. In the C 1s spectrum of GAC (Fig. 2B), the XPS peaks locating at 284.6, 285.5, 286.9 and

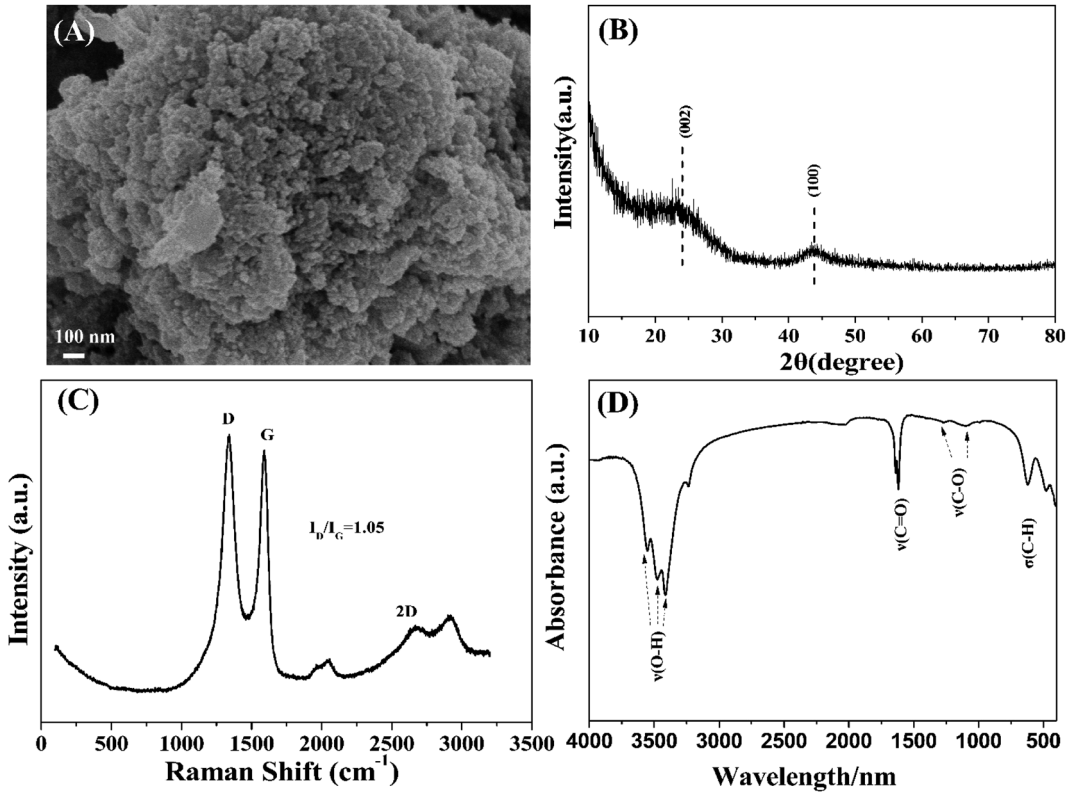

Fig. 1 Structural characterizations of GAC: (A) SEM image; (B) XRD pattern; (C) Raman spectrum; and (D) FTIR spectrum.

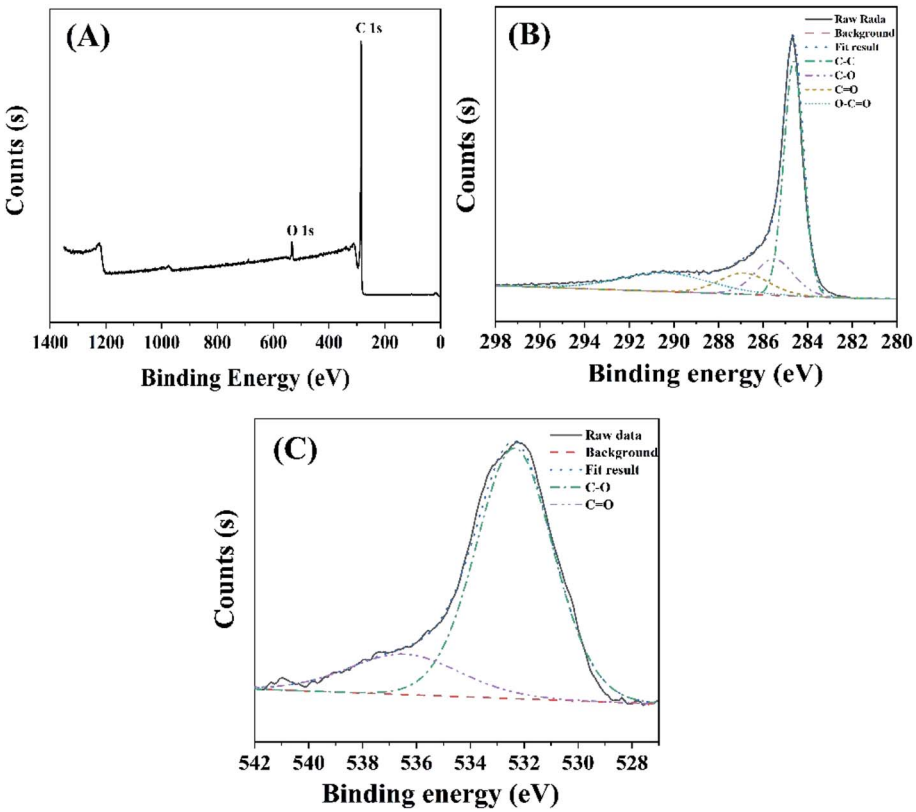

Fig. 2 (A) Survey XPS spectrum (B) C 1s spectrum; and (C) O 1s spectrum of GAC.

290.4 eV were registered in C–C/C–H, C–O, C═O and O–C═O bonds, respectively.[39] The O 1s spectra (Fig. 2C) divided into two peaks of 532.4 and 536.5 eV, indicating the presence of C–O and C═O bonds.[40] The results of XPS were identical with those of FTIR.

After modification, the structure of GAC was slightly changed. Table 1 lists the specific surface areas, pore volumes and pore sizes of GAC, GAC-S, GAC-HO, GAC-N and GAC-NH. The specific surface area of GAC was as high as 1782 $m^2\ g^{-1}$, which decreased to 1444 $m^2\ g^{-1}$ after treatment with 2 mol L^{-1} sulfuric acid, 1540 $m^2\ g^{-1}$ with 2 mol L^{-1} hydrogen peroxide, 1415 $m^2\ g^{-1}$ with 2 mol L^{-1} nitric acid, and 905 $m^2\ g^{-1}$ with 2 mol L^{-1} aminopropyl triethoxy silane. The oxidative treatment might diminish the specific surface area, which coincided with the previously published literature.[41] The same downward trends were observed in the microsurface area and pore volume. The drop in the specific surface area and pore volume may be caused by the blockage of some pores during the oxidative treatment.[42]

Fig. 3 shows the adsorption isotherms and the pore diameter distributions of the supports. As observed in Fig. 3A, all the adsorption isotherms for the supports belonged to the type IV hysteresis loops, indicating the presence of mesoporous pores.[43] The pore diameter distributions of the supports (Fig. 3B) suggested that the supports mainly consisted of the micropores. The most probable pore sizes of the supports were focused on the range of 0.5–0.6 nm.

After treatment, the surface of GAC was modified with the functional groups, which gradually decomposed and released CO or CO_2 gas with the increasing temperature under an inert gas atmosphere (*e.g.* He gas). Fig. 4A shows the He-TPD profiles of GAC, GAC-S, GAC-HO, GAC-N, and GAC-NH. As shown in

Table 1 Surface structural information of GAC supports treated with different reagents

Supports	BET ($m^2\ g^{-1}$)	Micropore area ($m^2\ g^{-1}$)	Pore volume ($cm^3\ g^{-1}$)	Micropore volume ($cm^3\ g^{-1}$)	Mean pore size (nm)	Mean micropore size (nm)
GAC	1782	832	1.03	0.37	2.32	0.54
GAC-S	1444	699	0.83	0.31	2.29	0.54
GAC-HO	1540	621	0.96	0.27	2.49	0.53
GAC-N	1415	757	0.78	0.34	2.19	0.53
GAC-NH	905	487	0.51	0.22	2.20	0.54

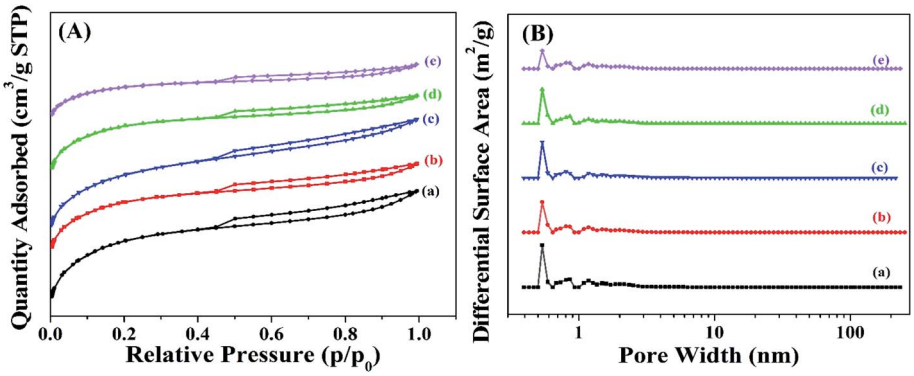

Fig. 3 (A) N_2 adsorption isotherms and (B) pore diameter distributions of (a) GAC, (b) GAC-S, (c) GAC-HO, (d) GAC-N, and (e) GAC-NH.

Fig. 4A(a), the peaks at 280 °C and 860 °C in the GAC He-TPD curve were attributed to the carboxylic acid group and the carbonyl substance, respectively.[44] Meanwhile, the distinct peak at 290 °C in the GAS-S He-TPD curve (Fig. 4A(b)) was also assigned to the carboxylic acid group and at 850 °C to the carbonyl substance. However, the peak at 290 °C was obviously larger than that of GAC, we speculated that the difference was derived from the sulfonic acid group. The He-TPD curve of GAC-HO (Fig. 4A(c)) was essentially the same as that of GAC, which indicated that the types of functional group remained unchanged after being treated with hydrogen peroxide. After functionalization with nitric acid, many peaks were observed in

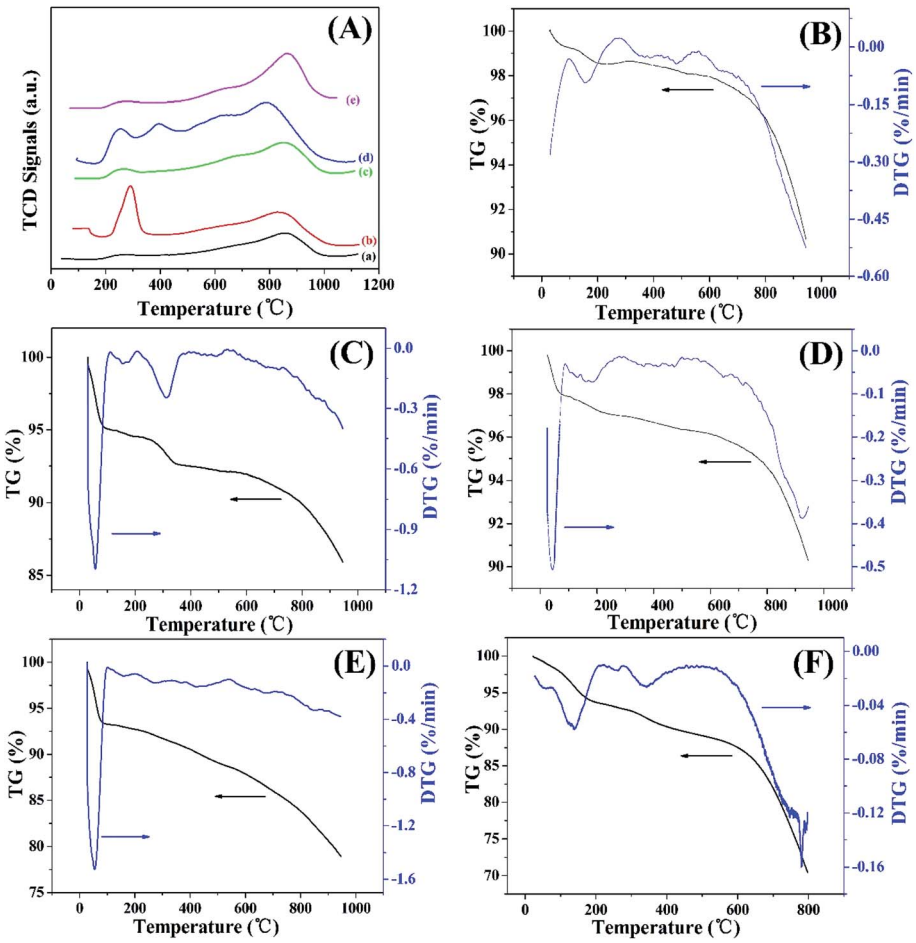

Fig. 4 (A) He-TPD of (a) GAC, (b) GAC-S, (c) GAC-HO, (d) GAC-N, and (e) GAC-NH; TG and DTG of (B) GAC, (C) GAC-S, (D) GAC-HO, (E) GAC-N, and (F) GAC-NH.

the He-TPD curve of GAC-N (Fig. 4A(d)), which suggested the fabrication of more functional groups, such as carboxylic groups, lactone, carboxylic anhydride groups, *etc.* The He-TPD curve of GAC-NH (Fig. 4A(e)) was almost the same as that of GAC, which indicated that the functional groups kept unchanged after being treated with aminopropyl triethoxy silane. Fig. 4B–F show the TGA and DTG curves of GAC, GAC-S, GAC-HO, GAC-N, and GAC-NH, respectively, which further revealed the surface functional groups of several carbon materials. As shown in Fig. 4B of the GAC TG and DTG profile, the exothermic peak (30–100 °C) was assigned to the evaporation of moisture. Furthermore, the peak at 155 °C was ascribed to the decomposition of carboxyl acid,[45] which was consistent with that of He-TPD and FTIR. Additionally, the weak peaks at 376 °C and 485 °C in the GAC DTG curve were attributed to the decomposition of the carboxyl anhydrides, and the one at 635 °C of the carbonyl group.[46] In the first stage (30–100 °C) of the TG curve of GAC-S (black line in Fig. 4C), the mass loss was also ascribed to the evaporation of moisture, which was shown at 57 °C of the DTG curve of GAC-S (blue line in Fig. 4C). Similar to GAC, the peak at 160 °C of the GAC-S DTG curve was attributed to the decomposition of carboxyl acid. The obvious peak at 312 °C in the GAC-S DTG curve was derived from the decomposition of the sulfonic acid group.[47] The weak peak at 490 °C in the GAC-S DTG curve was attributed to the decomposition of carboxyl anhydrides. As shown in Fig. 4D of the GAC-HO TG and DTG profile, the exothermic peak (30–100 °C) was assigned to the evaporation of moisture. The broad peaks in the regions of 90–280 °C and 284–500 °C were ascribed to the carboxyl acid and the carboxyl anhydrides, respectively. The peaks at 54 °C, 158 °C, 270 °C, 427 °C and 674 °C were attributed to the moisture, carboxyl acid, carboxyl anhydrides and carbonyl group, respectively (Fig. 4E), which was in agreement with the results of He-TPD. The peaks at 140 °C, 260 °C and 340 °C were assigned to the carboxyl acid, carboxyl anhydrides and amino group.[48]

Structural characterizations of the Pt-based catalysts

Fig. 5 shows the H_2-TPR curves of the GAC and Pt-based catalysts, which depicted the reduction mechanism. As shown in Fig. 5a, the peak at 630 °C was observed in the H_2-TPR curve of GAC, which was attributed to the surface functional groups of GAC. Compared with GAC, the H_2-TPR curve of Pt/GAC (Fig. 5b) showed the peaks at 240 °C and 340 °C, which were generated by the reduction of Pt–O–Pt and Pt–O–C,[49] respectively, further demonstrating the successful synthesis of Pt-based catalysts. The reduction peaks of Pt–O–Pt or Pt–O–C were also observed in the H_2-TPR curves of GAC-S (Fig. 5c), GAC-NH (Fig. 5d), GAC-HO (Fig. 5e), and GAC-N (Fig. 5f), which could improve the dispersion of the metal species. [50] Moreover, the reduction peaks in the curves of the Pt-based catalysts were less than 400 °C, which indicated that the Pt was in the metallic state in the catalysts before the dehydrogenation of MCH.

The degree of dispersion of the Pt particles affects the catalytic activity. The CO pulse adsorption was adopted to measure the degrees of dispersion of the Pt-based catalysts, which were listed in Table 2. The degrees of dispersion of the active

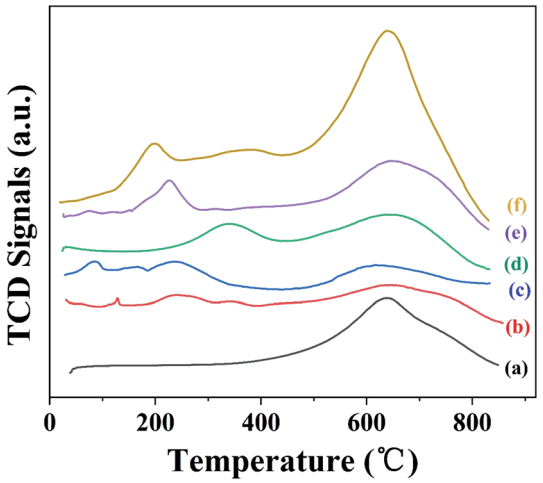

Fig. 5 H_2-TPR of (a) GAC, (b) Pt/GAC, (c) GAC-S, (d) GAC-NH, (e) GAC-HO, and (f) GAC-N.

component Pt in Pt/GAC, Pt/GAC-S, Pt/GAC-HO, Pt/GAC-N and Pt/GAC-NH were 26.6, 34.7, 20.3, 19.4 and 11%, respectively. In addition, the particle sizes of Pt were 4.26, 3.57, 5.58, 5.83 and 10.3 nm, respectively. The degree of dispersion of Pt/GAC-S was higher than that of Pt/GAC, and the particle size of Pt/GAC-S was smaller than that of Pt/GAC, which indicated that the activated carbon modified by dilute sulfuric acid effectively improved the dispersion of the Pt precursor and reduced the particle size. However, the degrees of dispersion of the Pt/GAC-HO, Pt/GAC-N and Pt/GAC-NH catalysts were lower than that of Pt/GAC, and the particle sizes of the Pt/GAC-HO, Pt/GAC-N and Pt/GAC-NH catalysts were much larger than that of Pt/GAC, demonstrating that hydrogen peroxide, dilute nitric acid and aminopropyl triethoxy silane were not conducive to the homodispersion of the Pt-based catalyst or improving the immersion load of chloroplatinic acid. In summary, the results showed that dilute sulfuric acid was a good reagent for improving the degree of dispersion of the precious metal Pt and reducing the particle size, which was consistent with the previously reported results.[51]

Dehydrogenation of MCH over the Pt-loaded catalysts

Fig. 6 shows the conversion curves of MCH to TOL and the hydrogen evolution histograms taking Pt/GAC, Pt/GAC-S, Pt/GAC-HO, Pt/GAC-N and Pt/GAC-NH as catalysts with a reaction temperature of 300 °C and a space velocity of 5 h^{-1}. As shown in Fig. 6A, the conversion of MCH using Pt/GAC as a catalyst was firstly about 21.2%, but dramatically decreased to 8.64% after 12 h, which might result from the agglomeration of the Pt/GAC catalyst. In contrast, the conversion of MCH adopting Pt/GAC-S as the catalyst was initially around 66.3% and slightly decreased to 61% after 12 h, which was higher and more stable than that of Pt/GAC. It might benefit from the high degree of dispersion and the small particle size of Pt/GAC-S. However, the conversion values of MCH utilizing Pt/GAC-HO, Pt/GAC-N, and Pt/GAC-NH as the catalysts were much lower than that of Pt/GAC, which indicated that dilute nitric acid,

Table 2 The CO pulse adsorption data for the Pt-loaded catalysts

Pt-based catalysts	Adsorption capacity of CO (μL CO g^{-1} catalyst)	Surface area of metal (m^2 g^{-1} sample)	Dispersion of active component (%)	Mean size of Pt (nm)
Pt/GAC	61.1	65.7	26.6	4.26
Pt/GAC-S	79.6	85.6	34.7	3.27
Pt/GAC-HO	46.6	50.1	20.3	5.58
Pt/GAC-N	44.7	48.0	19.4	5.83
Pt/GAC-NH	25.2	27.1	11.0	10.3

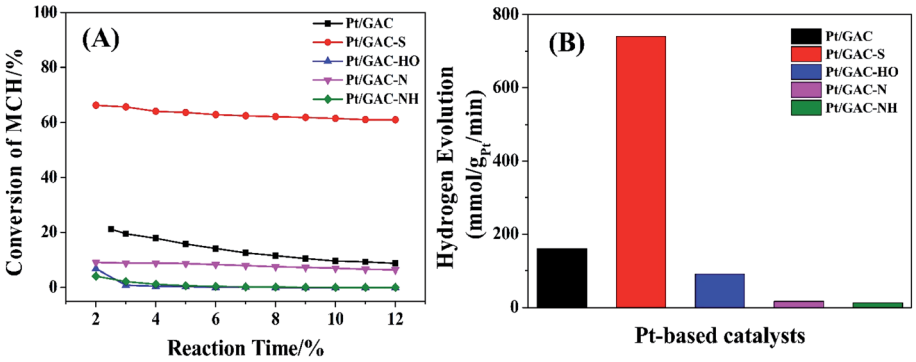

Fig. 6 (A) The conversion curves of MCH dehydrogenated into toluene and (B) hydrogen evolution histograms over Pt-based catalysts.

Table 3 Comparison of the dehydrogenation of MCH over previously reported Pt-based catalysts

Catalysts	Temperature (°C)	Rate of liquid MCH (mL min^{-1})	Catalyst weight	Pt loading content (wt%)	Conversion of MCH (%)	H_2 evolution rate (mmol g_{Pt}^{-1} min^{-1})	Ref.
Pt/SBA-15	300 °C	0.03	0.05	3	65 (initial)	305.8	52
Pt/Ce–Mg–Al–O	300 °C	—	—	0.35	49.8	686.9	53
Pt/coconut activated carbon	300 °C	0.03	0.03	1	42	592.9	54
Pt/pyrolytic waste activated carbon	300 °C	0.03	0.554	0.4	95	302.6	31
PtSn-5/Mg–Al–O-350	300 °C	0.1	0.5	2	90.5	212.9	55
Pt/GAC-S	300 °C	0.03	0.3	0.2	63	741.1	This work

hydrogen peroxide and aminopropyl triethoxy silane were not suitable for treating carbon materials to catalyze the dehydrogenation of MCH. The average conversion values of MCH utilizing Pt/GAC, PT/GAC-S, Pt/GAC-HO, Pt/GAC-N, and Pt/GAC-NH as the catalysts were 13.6%, 63.0%, 7.78%, 1.41% and 1.09%, respectively, which were exploited to calculate the hydrogen evolution (Fig. 6B). The hydrogen evolution rate of Pt/GAC was 160.2 mmol g_{Pt}^{-1} min^{-1}, which increased up to 741.1 mmol g_{Pt}^{-1} min^{-1} of Pt/GAC-S, further indicating the good catalytic activity of Pt/GAC-S in the dehydrogenation of MCH. However, the hydrogen evolution rates of Pt/GAC-HO, Pt/GAC-N, and Pt/GAC-NH were obviously less than that of Pt/GAC, which proved their poor catalytic abilities in the dehydrogenation of MCH. Table 3 lists a comparison of the dehydrogenation of MCH on catalysts previously reported in the literature, which showed that the hydrogen evolution rate in this work was higher than previously reported results, further indicating the good performance of the resultant Pt/GAC-S for the catalytic dehydrogenation of MCH.

Fig. S1† displays the Pt 4f XPS spectra and S 2p XPS spectra of the fresh and the recovered Pt/GAC-S catalysts. As revealed in Fig. S1A,† two-doublet binding energies in the Pt $4f_{7/2}$ spectra of the fresh Pt/GAC-S catalyst were obtained. The peaks at 70.4 and 73.1 eV were attributed to metallic platinum and PtO, corresponding to Pt(0) and Pt(II), respectively.[56] 76.1 and 79.9 eV in the Pt $4f_{5/2}$ spectra of the fresh Pt/GAC-S catalyst were assigned to Pt(0) and Pt(II), respectively. Compared to the fresh Pt/GAC-S, the doublets binding energies in the Pt $4f_{7/2}$ and $4f_{5/2}$ spectra of the recovered Pt/GAC-S catalyst were almost unchanged. The peaks at 70.0 eV in the Pt $4f_{7/2}$ spectra and 75.9 eV in the Pt $4f_{5/2}$ spectra resulted from metallic platinum, while that of 73.0 eV in the Pt $4f_{7/2}$ spectra and 80.2 eV in the Pt $4f_{5/2}$ spectra were caused by PtO. Fig. S1B† presents the decomposition curves of the S 2p spectra in fresh and the recovered Pt/GAC-S catalysts.

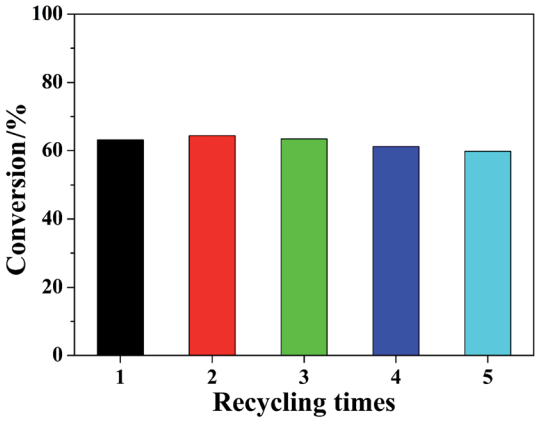

Fig. 7 Recycling studies for the Pt/GAC-S catalyst.

The doublets located at 164.4 eV of the fresh Pt/GAC-S catalyst and 164.7 eV of the recovered Pt/GAC-S catalyst were assigned to oxysulfide,[57] and the ones at 169.1 eV of the fresh Pt/GAC-S catalyst and 169.3 eV of the recovered Pt/GAC-S catalyst were attributed to the sulfate species,[58] which further proved the successful functionalization of GAC by dilute sulphuric acid. Fig. 7 demonstrates the results of the recycling assays. The conversions of MCH was observed a small fluctuation in the range of 59.8–64.4%, which showed that the activities of Pt/GAC-S hardly decreased after being reused four times, indicating the good stability of the Pt/GAC-S catalyst. After the first run, Pt leaching in the reaction was 0.32 ppm (measured by ICP-AES). When the Pt catalyst was filtrated from the reaction system, the catalytic reaction was seldom observed in the filtrate, which proved that the Pt on carbon supports acted as the heterogeneous active sites.

Conclusions

Herein, we developed the dehydrogenation of MCH over Pt-based catalysts supported on functional GAC. Sulphuric acid, hydrogen peroxide, nitric acid and aminopropyl triethoxy silane were utilized to modify GAC to yield GAC-S, GAC-HO, GAC-N, and GAC-NH supports. Characterizations including SEM, FTIR, N_2-adsorption, XPS and TGA suggested that the as-prepared functional carbon supports had a large surface area, abundant pore structure, and a significant number of oxygen-containing functional groups. The results of H_2-TPR analysis demonstrated the interaction between the active component Pt and the various functionalized carbon supports. CO pulse data revealed that Pt/GAC-S showed a smaller particle size and a higher dispersion than the other Pt-based catalysts. The catalytic activities of the Pt-based catalysts were finally studied in the dehydrogenation reaction of MCH. Recycling studies indicated the good stability of the Pt/GAC-S catalyst and the heterogeneous active sites of Pt component. The results of the catalytic reaction showed that the Pt/GAC-S catalyst demonstrated a higher conversion of MCH (63%) and a larger hydrogen evolution rate (741.1 mmol g_{Pt}^{-1} min^{-1}) than the other resulting Pt-based catalysts at 300 °C.

Author contributions

Hong-Li Ye: conceptualization, investigation, methodology, data curation, writing – original draft; **Shuang-Xi Liu**: investigation, data curation; **Cui Zhang**: supervision, writing – review and editing, funding acquisition, project administration; **You-Qiong Cai**: supervision, writing – review and editing; **Yong-Fu Shi**: supervision, writing – review and editing.

Conflicts of interest

There are no conflicts of interest to declare.

Acknowledgements

This work was supported by the National Natural Science Foundation of China [no. 21003077] and the Key Project of Tianjin Application Foundation and Frontier Plan [no. 14JCZDJC32000].

References

1 D. D. Chen, C. Han, Q. H. Sun, J. Y. Ding, Q. Huang, T. T. Li, Y. Hu, J. J. Qian and S. M. Huang, Bimetallic AgNi nanoparticles anchored onto MOF-derived nitrogen-doped carbon nanostrips for efficient hydrogen evolution, *Green Energy Environ.*, 2021, DOI: 10.1016/j.gee.2021.04.003.
2 H. Lee, A. Kim, B. Lee and H. Lim, Comparative numerical analysis for an efficient hydrogen production *via* a steam methane reforming with a packed-bed reactor, a membrane reactor, and a sorption-enhanced membrane reactor, *Energy Convers. Manage.*, 2020, **213**, 112839, DOI: 10.1016/j.enconman.2020.112839.
3 M. Burhan, M. W. Shahzad, S. J. Oh and K. C. Ng, A pathway for sustainable conversion of sunlight to hydrogen using proposed compact CPV system, *Energy Convers. Manage.*, 2018, **165**, 102–112, DOI: 10.1016/j.enconman.2018.03.027.
4 Z. Li, Z. H. Yao, A. A. Haidry, T. Plecenik, B. Grancic, T. Roch, M. Gregor and A. Plecenik, The effect of Nb doping on hydrogen gas sensing properties of capacitor-like Pt/Nb-TiO_2/Pt hydrogen gas sensors, *J. Alloys Compd.*, 2019, **806**, 1052–1059, DOI: 10.1016/j.jallcom.2019.07.301.
5 A. Mohammadi and M. Mehrpooya, Techno-economic analysis of hydrogen production by solid oxide electrolyzer coupled with dish collector, *Energy Convers. Manage.*, 2018, **173**, 167–178, DOI: 10.1016/j.enconman.2018.07.073.
6 Y. K. Salkuyeh, B. A. Saville and H. L. MacLean, Techno-economic analysis and life cycle assessment of hydrogen production from natural gas using current and emerging technologies, *Int. J. Hydrogen Energy*, 2017, **42**, 18894–18909, DOI: 10.1016/j.ijhydene.2017.05.219.
7 Q. L. Zhu and Q. Xu, Liquid organic and inorganic chemical hydrides for high-capacity hydrogen storage, *Energy Environ. Sci.*, 2015, **8**, 478–512, DOI: 10.1039/C4EE03690E.
8 N. Kariya, A. Fukuoka and M. Ichikawa, Efficient evolution of hydrogen from liquid cycloalkanes over Pt-containing catalysts supported on active carbons under "wet-dry

multiphase conditions", *Appl. Catal., A*, 2002, **233**, 91–102, DOI: 10.1016/S0926860X(02)-001394.

9 Z. Kou, Z. Zhi, G. Xu, Y. An and C. He, Investigation of the performance and deactivation behavior of Raney-Ni catalyst in continuous dehydrogenation of cyclohexane under multiphase reaction conditions, *Appl. Catal., A*, 2013, **467**, 196–201, DOI: 10.1016/j.apcata.2013.07.025.

10 J. F. Li, Y. M. Chai, B. Liu, Y. L. Wu, X. H. Li, Z. Tang, Y. Q. Liu and C. G. Liu, The catalytic performance of Ni_2P/Al_2O_3 catalyst in comparison with Ni/Al_2O_3 catalyst in dehydrogenation of cyclohexane, *Appl. Catal., A*, 2014, **469**, 434–441, DOI: 10.1016/j.apcata.2013.09.047.

11 F. T. Chen, Y. P. Huang, C. J. Mi, K. Wu, W. Y. Wang, W. S. Li and Y. Q. Yang, Density functional theory study on catalytic dehydrogenation of methylcyclohexane on Pt (111), *Int. J. Hydrogen Energy*, 2020, **45**, 6727–6737, DOI: 10.1016/j.ijhydene.2019.12.096.

12 A. H. Zahid, N. Amin, F. Nisar and S. Saghir, Analysis of MTH-System (Methylcyclohexane-Toluene-Hydrogen-System) for hydrogen production as fuel for power plants, *Int. J. Hydrogen Energy*, 2020, **45**, 32234–32242, DOI: 10.1016/j.ijhydene.2020.08.248.

13 A. A. Shukla, P. V. Gosavi, J. V. Pande, V. P. Kumar, K. V. R. Chary and R. B. Biniwale, Efficient hydrogen supply through catalytic dehydrogenation of methylcyclohexane over Pt/metal oxide catalysts, *Int. J. Hydrogen Energy*, 2010, **35**, 4020–4026, DOI: 10.1016/j.ijhydene.2010.02.014.

14 L. Miao, J. Yan, W. Y. Wang, Y. P. Huang, W. S. Li and Y. Q. Yang, Dehydrogenation of methylcyclohexane over Pt supported on Mg-Al mixed oxides catalyst: The effect of promoter Ir, *Chin. J. Chem. Eng.*, 2020, **28**, 2337–2342, DOI: 10.1016/j.cjche.2020.05.026.

15 Y. Sugiura, T. Nagatsuka, K. Kubo, Y. Hirano, A. Nakamura, K. Miyazawa, Y. Iizuka, S. Furuta, H. Iki, T. Higo and Y. Sekine, Dehydrogenation of methylcyclohexane over Pt/TiO_2-Al_2O_3 catalysts, *Chem. Lett.*, 2017, **46**, 1601–1604, DOI: 10.1246/cl.170722.

16 G. M. Pajonk, Contribution of spillover effects to heterogeneous catalysis, *Appl. Catal., A*, 2000, **202**, 157–169, DOI: 10.1016/S0926-860X(00)00522-6.

17 Q. Huang, Y. Y. Guo, D. D. Chen, L. J. Zhang, T. T. Li, Y. Hu, J. J. Qian and S. M. Huang, Rational construction of ultrafine noble metals onto carbon nanoribbons with efficient oxygen reduction in practical alkaline fuel cell, *Chem. Eng. J.*, 2021, **424**, 130336, DOI: 10.1016/j.cej.2021.130336.

18 M. R. Usman, F. M. Alotaibi and R. Aslam, Dehydrogenation-hydrogenation of methylcyclohexane-toluene system on 1.0 wt% Pt/zeolite beta catalyst, *Prog. React. Kinet. Mech.*, 2015, **40**, 353–366, DOI: 10.3184/146867815X14413752286029.

19 S. Karthikeyan, M. P. Pachamuthu, M. A. Isaacs, S. Kumar, A. F. Lee and G. Sekaran, Cu and Fe oxides dispersed on SBA-15: A Fenton type bimetallic catalyst for *N*,*N*-diethyl-*p*-phenyl diamine degradation, *Appl. Catal., B*, 2016, **199**, 323–330, DOI: 10.1016/j.apcatb.2016.06.040.

20 L. Deng, T. Arakawa, T. Ohkubo, H. Miura, T. Shishido, S. Hosokawa, K. Teramura and T. Tanaka, Highly active and stable Pt-Sn/SBA-15 catalyst prepared by direct reduction for ethylbenzene dehydrogenation: effects of Sn addition, *Ind. Eng. Chem. Res.*, 2017, **56**, 7160–7172, DOI: 10.1021/acs.iecr.7b01598.

21 A. I. Osman, J. K. Abu-Dahrieh, N. Cherkasov, J. Fernandez-Garcia, D. Walker, R. I. Walton, D. W. Rooney and E. Rebrov, A highly active and synergistic $Pt/Mo_2C/Al_2O_3$ catalyst for water-gas shift reaction, *Mol. Catal.*, 2018, **455**, 38–47, DOI: 10.1016/j.mcat.2018.05.025.

22 K. O. Obodo, C. N. M. Ouma, P. M. Modisha and D. Bessarabov, Density functional theory calculation of Ti_3C_2 MXene monolayer as catalytic support for platinum towards the dehydrogenation of methylcyclohexane, *Appl. Surf. Sci.*, 2020, **529**, 147186, DOI: 10.1016/j.apsusc.2020.147186.

23 X. Wang, A. R. Dong, Z. Y. Zhu, L. L. Chai, J. Y. Ding, L. Zhong, T. T. Li, Y. Hu, J. J. Qian and S. M. Huang, Surfactant-Mediated Morphological Evolution of MnCo Prussian Blue Structures, *Small*, 2020, **16**, 2004614, DOI: 10.1002/smll.202004614.

24 J. Wang, H. Liu, S. G. Fan, W. N. Li, Z. Li, H. R. Yun, X. Xu, A. J. Guo and Z. X. Wang, Size-dependent catalytic cyclohexane dehydrogenation with platinum nanoparticles on nitrogen-doped carbon, *Energy Fuels*, 2020, **34**, 16542–16551, DOI: 10.1021/acs.energyfuels.0c03085.

25 P. D. Tien, T. Satoh, M. Miura and M. Nomura, Continuous hydrogen evolution from cyclohexanes over platinum catalysts supported on activated carbon fibers, *Fuel Process. Technol.*, 2008, **89**, 415–418, DOI: 10.1016/j.fuproc.2007.11.010.

26 H. Kong, M. Zhou, G. D. Lin and H. B. Zhang, Pt catalyst supported on multi-walled carbon nanotubes for hydrogenation-dearomatization of toluene and tetralin, *Catal. Lett.*, 2010, **135**, 83–90, DOI: 10.1007/s10562-010-0272-9.

27 Z. Jiang, S. Guo and T. Fang, Enhancing the catalytic activity and selectivity of $PdAu/SiO_2$ bimetallic catalysts for dodecahydro-*N*-ethylcarbazole dehydrogenation by controlling the particle size and dispersion, *ACS Appl. Energy Mater.*, 2019, **2**, 7233–7243, DOI: 10.1021/acsaem.9b01202.

28 Y. G. Wang, N. Shah and G. P. Huffman, Pure hydrogen production by partial dehydrogenation of cyclohexane and methylcyclohexane over nanotube-supported Pt and Pd catalysts, *Energy Fuels*, 2004, **18**, 1429–1433, DOI: 10.1021/ef049959o.

29 R. Viscardi, V. Barbarossa, R. Maggi and F. Pancrazzi, Effect of acidic MCM-41 mesoporous silica functionalized with sulfonic acid groups catalyst in conversion of methanol to dimethyl ether, *Energy Rep.*, 2020, **6**, 49–55, DOI: 10.1016/j.egyr.2020.10.042.

30 M. S. Hosseini, M. M. Farahani and S. Shahsavarifar, Chemical modification of re duce d graphene oxide with sulfonic acid groups: Efficient solid acids for acetalization

and esterification reactions, *J. Taiwan Inst. Chem. Eng.*, 2019, **102**, 34–43, DOI: 10.1016/j.jtice.2019.05.020.

31 C. Zhang, X. Q. Liang and S. X. Liu, Hydrogen production by catalytic dehydrogenation of methylcyclohexane over Pt catalysts supported on pyrolytic waste tire char, *Int. J. Hydrogen Energy*, 2011, **36**, 8902–8907, DOI: 10.1016/j.ijhydene.2011.04.175.

32 Z. H. Pu, M. Wang, Z. K. Kou, I. S. Amiinu and S. C. Mu, Mo_2C quantum dot embedded chitosan-derived nitrogen-doped carbon for efficient hydrogen evolution in a broad pH range, *Chem. Commun.*, 2016, **52**, 12753–12756, DOI: 10.1039/c6cc06267a.

33 J. Y. Wang, T. Ouyang, Y. P. Deng, Y. S. Hong and Z. Q. Liu, Metallic Mo_2C anchored pyrrolic-N induced N-CNTs/NiS_2 for efficient overall water electrolysis, *J. Power Sources*, 2019, **420**, 108–117, DOI: 10.1016/j.jpowsour.2019.02.098.

34 N. Przybylska, M. Śliwińska-Bartkowiak, M. Kościński, K. Rotnicki, M. Bartkowiak and S. Jurga, Confined effect of water solution of ciprofloxacin in carbon nanotubes studied by Raman and Fourier Transform Infrared Spectroscopy methods, *J. Mol. Liq.*, 2021, **336**, 115938, DOI: 10.1016/j.molliq.2021.115938.

35 Y. L. Zhong, X. T. Sun, S. Y. Wang, F. Peng, F. Bao, Y. Y. Su, Y. Y. Li, S. T. Lee and Y. He, Facile, large-quantity synthesis of stable, tunable-color silicon nanoparticles and their application for long-term cellular imaging, *ACS Nano*, 2015, **9**, 5958–5967, DOI: 10.1021/acsnano.5b00683.

36 S. Zhu, L. Wang, B. Li, Y. Song, X. Zhao, G. Zhang, S. Zhang, S. Lu, J. Zhang, H. Wang, H. Sun and B. Yang, Investigation of photoluminescence mechanism of graphene quantum dots and evaluation of their assembly into polymer dots, *Carbon*, 2014, **77**, 462–472, DOI: 10.1016/j.carbon.2014.05.051.

37 H. Ding, S. B. Yu, J. S. Wei and H. M. Xiong, Full-color light-emitting carbon dots with a surface-state-controlled luminescence mechanism, *ACS Nano*, 2016, **10**, 484–491, DOI: 10.1021/acsnano.5b05406.

38 X. D. Tang, H. M. Yu, B. Bui, L. Y. Wang, C. Xing, S. Y. Wang, M. L. Chen, Z. Z. Hu and W. Chen, Nitrogen-doped fluorescence carbon dots as multi-mechanism detection for iodide and curcumin in biological and food samples, *Bioact. Mater.*, 2021, **6**, 1541–1554, DOI: 10.1016/j.bioactmat.2020.11.006.

39 H. J. Zhang, Y. L. Chen, M. J. Liang, L. F. Xu, S. D. Qi, H. L. Chen and X. G. Chen, Solid-phase synthesis of highly fluorescent nitrogen-doped carbon dots for sensitive and selective probing ferric ions in living cells, *Anal. Chem.*, 2014, **86**, 9846–9852, DOI: 10.1021/ac50244-6m.

40 S. D. Ma, Y. L. Chen, J. Feng, J. J. Liu, X. W. Zuo and X. G. Chen, One-step synthesis of water-dispersible and biocompatible silicon nanoparticles for selective heparin sensing and cell imaging, *Anal. Chem.*, 2016, **88**, 10474–10481, DOI: 10.1021/acs.analchem.6b02448.

41 L. G. Pyanova, L. S. Luzyanina, V. A. Drozdov, A. V. Veselovskaya, A. B. Arbuzov and V. A. Likholobov, Study of the effect of a number of oxidizers on variation of composition of surface functional groups, porous structure, and adsorption properties of composite carbon-carbon sorbent, *Prot. Met. Phys. Chem. Surf.*, 2010, **46**, 320–324, DOI: 10.1134/S2070205110030056.

42 K. N. Iost, V. A. Borisov, V. L. Temerev, Y. V. Surovikin, P. E. Pavluchenko, M. V. Trenikhin, A. B. Arbuzov, D. A. Shlyapin, P. G. Tsyrulnikov and A. A. Vedyagin, Mechanism of Pt interfacial interaction with carbonaceous support under reductive conditions, *React. Kinet., Mech. Catal.*, 2019, **127**, 103–115, DOI: 10.1007/s11144-019-01554-4.

43 B. Qi, Y. B. Wang, L. L. Lou, L. Y. Huang, Y. Yang and S. X. Liu, Solvent-free aerobic oxidation of alcohols over palladium supported on MCM-41, *J. Mol. Catal. A: Chem.*, 2013, **370**, 95–103, DOI: 10.1016/j.molcata.2013.01.007.

44 D. A. Bulushev, I. Yuranov, E. I. Suvorova, P. A. Buffat and L. K. Minsker, Highly dispersed gold on activated carbon fibers for low-temperature CO oxidation, *J. Catal.*, 2004, **224**, 8–17, DOI: 10.1016/j.jcat.2004.02.014.

45 J. L. Figueiredo, Functionalization of porous carbons for catalytic applications, *J. Mater. Chem. A*, 2013, **1**, 9351–9364, DOI: 10.1039/c3ta10876g.

46 Y. W. Huang, Q. F. Yua, M. Li, S. X. Jin, J. Fan, L. Zhao and Z. H. Yao, Surface modification of activated carbon fiber by low-temperature oxygen plasma: Textural property, surface chemistry, and the effect of water vapor adsorption, *Chem. Eng. J.*, 2021, **418**, 129474, DOI: 10.1016/j.cej.2021.129474.

47 H. G. Tsai, P. J. Chiu, G. L. Jheng, C. C. Ting, Y. C. Pan and H. M. Kao, Synthesis and solid-state NMR characterization of cubic mesoporous silica SBA-1 functionalized with sulfonic acid groups, *J. Colloid Interface Sci.*, 2011, **359**, 86–94, DOI: 10.1016/j.jcis.2011.03.072.

48 H. P. Chen, Y. P. Xie, W. Chen, M. W. Xia, K. X. Li, Z. Q. Chen, Y. Q. Chen and H. P. Yang, Investigation on co-pyrolysis of lignocellulosic biomass and amino acids using TG-FTIR and Py-GC/MS, *Energy Convers. Manage.*, 2019, **196**, 320–329, DOI: 10.1016/j.enconman.2019.06.010.

49 X. Yang, Y. Song, T. T. Cao, L. Wang, H. T. Song and W. Lin, The double tuning effect of TiO_2 on Pt catalyzed dehydrogenation of methylcyclohexane, *Mol. Catal.*, 2020, **492**, 110971, DOI: 10.1016/j.mcat.2020.110971.

50 C. Bittencourt, M. Hecq, A. Felten, J. J. Pireaux, J. Ghijsen, M. P. Felicissimo, P. Rudolf, W. Drube, X. Ke and T. G. Van, Platinum-carbon nanotube interaction, *Chem. Phys. Lett.*, 2008, **462**, 260–264, DOI: 10.1016/j.cplett.2008.07.082.

51 J. Machado, J. E. Castanheiro, I. Matos, A. M. Ramos, J. Vital and I. M. Fonseca, SBA-15 with sulfonic acid groups as a Green Catalyst for the acetoxylation of α-pinene, *Microporous Mesoporous Mater.*, 2012, **163**, 237–242, DOI: 10.1016/j.micromeso.2012.07.028.

52 A. Chen, W. Zhang, X. Li, D. Tan, X. Han and X. Bao, One-pot encapsulation of Pt nanoparticles into the mesochannels of SBA-15 and their catalytic dehydrogenation of methylcyclohexane, *Catal. Lett.*, 2007, **119**, 159–164, DOI: 10.1007/s10562-007-9214-6.

53 W. Y. Wang, L. Miao, K. Wu, G. L. Chen, Y. P. Huang and Y. Q. Yang, Hydrogen evolution in the dehydrogenation of

methylcyclohexane over Pt/Ce Mg Al O catalysts derived from their layered double hydroxides, *Int. J. Hydrogen Energy*, 2019, **44**, 2918–2925, DOI: 10.1016/j.ijhydene.2018.12.072.

54 J. Yan, W. Y. Wang, L. Miao, K. Wu, G. L. Chen, Y. P. Huang and Y. Q. Yang, Dehydrogenation of methylcyclohexane over Pt–Sn supported on Mg–Al mixed metal oxides derived from layered double hydroxides, *Int. J. Hydrogen Energy*, 2018, **43**, 9343–9352, DOI: 10.1016/j.ijhydene.2018.04.003.

55 X. Y. Li, D. Ma and X. H. Bao, Dispersion of Pt catalysts supported on activated carbon and their catalytic performance in methylcyclohexane dehydrogenation, *Chin. J. Catal.*, 2008, **29**, 259–263, DOI: 10.1016/S1872-2067(08)60027-3.

56 M. Y. Smirnov, A. V. Kalinkin, E. I. Vovk, P. A. Simonov, E. Y. Gerasimov, A. M. Sorokin and V. I. Bukhtiyarov, Comparative XPS study of interaction of model and real Pt/C catalysts with NO_2, *Appl. Surf. Sci.*, 2018, **428**, 972–976, DOI: 10.1016/j.apsusc.2017.09.205.

57 L. M. Qiu and G. T. Xu, Peak overlaps and corresponding solutions in theX-ray photoelectron spectroscopic study of hydrodesulfurization catalysts, *Appl. Surf. Sci.*, 2010, **256**, 3413–3417, DOI: 10.1016/j.apsusc.2009.12.043.

58 L. M. Qiu, K. Zou and G. T. Xu, Investigation on the sulfur state and phase transformation of spent and regenerated S zorb sorbents using XPS and XRD, *Appl. Surf. Sci.*, 2013, **266**, 230–234, DOI: 10.1016/j.apsusc.2012.11.156.